IEEE Access
Multidisciplinary | Rapid Review | Open Access Journal

Received March 4, 2019, accepted March 17, 2019, date of publication March 25, 2019, date of current version April 8, 2019.

Digital Object Identifier 10.1109/ACCESS.2019.2907193

Modeling and Control of Underwater Mine Explorer Robot UX-1

RAMON A. SUAREZ FERNANDEZ[1], DAVIDE GRANDE[2,3], ALFREDO MARTINS[3], LUCA BASCETTA[2], SERGIO DOMINGUEZ[1], AND CLAUDIO ROSSI[1]

[1]Centre for Automation and Robotics, Universidad Politécnica de Madrid, 28006 Madrid, Spain
[2]Dipartimento di Elettronica, Informazione e Bioingegneria, Politecnico di Milano, 20133 Milan, Italy
[3]INESC Technology and Science, INESC-TEC, 4200-072 Porto, Portugal

Corresponding author: Ramon A. Suarez Fernandez (fernandez.suarez.ramon@gmail.com)

This work was supported in part by the UNEXMIN Project through the European Union's Horizon 2020 Research and Innovation Programme under Agreement 690008, in part by the RoboCity2030-DIH-CM Madrid Robotics Digital Innovation Hub (Robotica aplicada a la mejora de la calidad de vida de los ciudadanos. fase IV) through the Programas de Actividades I+D en la Comunidad de Madrid under Grant S2018/NMT-4331, and in part by the Structural Funds of the EU.

ABSTRACT This paper presents the design and experimental assessment of the control system for the UX-1 robot, a novel spherical underwater vehicle for flooded mine tunnel exploration. Propulsion and maneuvering are based on an innovative manifold system. First, the overall design concepts of the robot are presented. Then, a theoretical six degree-of-freedom (DOF) dynamic model of the system is derived. Based on the dynamic model, two control systems have been developed and tested, one based on the principle of nonlinear state feedback linearization and another based on a finite horizon linear quadratic regulator (LQR). A series of experimental tests have been carried out in a controlled environment to experimentally identify the complex parameters of the dynamic model. Furthermore, the two proposed controllers have been tested in underwater path tracking experiments designed to simulate navigation in mine tunnel environments. The experimental results demonstrated the effectiveness of both the proposed controllers and showed that the state feedback linearization controller outperforms the finite horizon LQR controller in terms of robustness and response time, while the LQR appears to be superior in terms of fall time.

INDEX TERMS AUV, mine exploration, robot control, spherical robot, UNEXMIN.

I. INTRODUCTION

Europe has almost complete dependency on the import of mineral raw materials. Some of these minerals, which were disregarded during the operational life of mine sites (such as germanium in some lead/zinc mines), are now considered ''critical minerals'' and are in high demand [1]. Paradoxically, an estimated 30,000 mining sites still contain raw materials, such as metallic and industrial minerals, construction materials, or base metals. Nevertheless, such mining sites are currently closed and/or abandoned, many of them more than one century ago.

The closure of these mines was commonly related to economic, environmental, and technological challenges more than the actual presence of mineral resources. However, new mining technologies, as well as an increased economic pressure, have raised the interest for re-opening some of these abandoned mine sites. Most of these old mine sites are nowadays flooded, and the information available regarding the structural layout of the tunnels is limited or imprecise. In order to take re-opening into consideration, surveying and prospecting the mine tunnels network should be conducted.

Exploration by human divers, however, is ruled out due to the risks involved, and de-watering without a priori knowledge of the mineralogical composition is impossible because of its high costs. Therefore, the use of robotic systems, predominantly Unmanned Underwater Vehicles (UUVs), appears to be the main choice for current research endeavors. The UNEXMIN project [2], proposes the design and use of an innovative non-invasive fully autonomous underwater robot, hereby named UX-1, for the exploration and mapping of flooded mines.

Due to the particular environmental constraints (tunnel cross-sections are in the range of 1.5m x 2m to 3m x 3m) and the possible presence of objects and debris from infrastructures left after closure, a spherical shape is adopted with an

The associate editor coordinating the review of this manuscript and approving it for publication was Gongbo Zhou.

embedded thruster configuration (''manifolds'', see Fig. 2), that minimizes the number of moving parts and protruding elements, whilst allowing high stability and maneuverability.

Another important issue that has to be solved is the design of the navigation system. In fact, the control of such vehicles is a rather complex and challenging task. For this reason this paper proposes two control solutions that have been developed in the framework of the UNEXMIN project, and are thus specific for the considered underwater vehicle and for the requirements of the flooded mine navigation task. In particular, considering that UX-1 is characterized by a highly nonlinear motion model whose coefficients, especially the ones related to the hydrodynamic effects, are difficult to identify and affected by uncertainty, two different control strategies have been developed. The first one, based on a linear approximation of the motion model, exploits Linear Quadratic control theory to derive a position/velocity controller in a cascaded-control architecture. Though the navigation inside a flooded mine is characterized by low velocities, and the linear approximation seems to be acceptable, experimental results have revealed the limitations of this approach.

For this reason, a second control strategy has been developed, introducing an exact linearization of the motion model based on a feedback linearization controller. In this way the outer loop can be still designed using linear control theory, but avoiding the introduction of any approximation. Furthermore, despite the aforementioned model uncertainties that can represent a critical issue in the case of a feedback linearizing law, experimental results clearly demonstrate the effectiveness of this approach. It must be also noticed that the solution here presented opens the way to further developments, as the outer loop can be designed using different and more complex/powerful control strategies, like for example Model Predictive Control (MPC).

A. RELATED WORK

In recent years, robotics researchers have shown a growing interest in underwater vehicles, though, most of the commercially sold UUVs in the market are only available as remotely operated. This limits the possible applications, because of high operational costs and safety regulations [3]. Hence, there have been increased efforts to design and develop self-contained, small-sized, and intelligent Autonomous Underwater Vehicles (AUVs).

There are countless possible applications for AUVs. Environmental applications include data gathering [4], [5] and autonomous sea floor mapping [6], [7]. Military applications, such as mine countermeasures, make use of intervention AUVs that have the capability of searching, locating, and manipulating underwater objects of interest [8], [9]; whilst Ocean Mining applications make use of AUVs, such as HUGIN, to map deepwater oil and gas fields [10]. Nevertheless, most of the development in underwater robotics for these type of applications is intended for open water scenarios, where the restrictions on shapes and sizes of the vehicle are not rigorous, unlike the underwater mine tunnel environments contemplated in the UNEXMIN project.

Consequently, a spherical design where high stability and flexibility can be obtained along with a zero degree turn radius for high maneuverability is proposed for the UX-1 robot. To the best of our knowledge, only few works can be found in the literature focusing on spherical UUVs. A μAUV of 0.075m radius and 6 propellers around the hull was developed by the authors of [11] and [12] for monitoring nuclear storage ponds. The authors in [13], [14], and [15] make use of the spherical UUV SUR-II, which is equipped with water-jet thrusters as propulsion, to design and develop attitude stabilization methods as well as buoyancy control with a variable ballast tank. In [16], the underwater robot ODIN-III is presented. It has a hollow metal sphere housing of 0.63m in diameter and a propulsion system that consisted of 8 thrusters fixed outside the hull.

FIGURE 1. Proposed spherical underwater vehicle prototype during pool tests.

One key disadvantage of these UUV designs is the presence of external propulsion systems, which could become entangled with objects such as ropes or cables encountered during operation. Taking into account the benefits and drawbacks of these systems, the design proposed in this work (Fig. 1), integrates the propulsion elements into the spherical hull to avoid foreign objects from damaging the propellers and effectively eliminating the possibility of ensnarement. Works related to the control of UX-1 includes [17] in which a scaled prototype is developed as a testing and validating platform for control systems in shallow water tanks.

B. OUTLINE OF THE PAPER

This work is organized as follows: Section II introduces the general design aspects of the robot, while in Section III the 6 degree-of-freedom (DOF) equations of motion for an UUV are derived. Section IV introduces the proposed control system, whilst underwater experimental tests are reported in

FIGURE 2. Final 3D model of robot mechanical design (a) Left view (manifold system for propulsion and scientific imaging equipment), (b) front view (M3 Sonar and structured light systems), (c) right view (manifold system and camera).

Section V. Finally, results and discussions are carried out in Section VI with conclusions and future works presented in Section VII.

II. ROBOT DESIGN

The robot was designed to be a mine exploring spherical underwater vehicle; thus, given the challenging environments in which the will have to operate, strict design restrictions and requirements have had to be observed. The final robot design, presented in Fig. 2, has been recently presented in several works, such as [18] and [19]; however, for the readers' understanding, the following sections briefly introduce the main elements of the robot.

A. MECHANICAL DESIGN

1) EXTERNAL HULL & MANIFOLDS

The external pressure hull, shown in Fig. 3, has a diameter of approximately 0.65m and is assembled by three components: a toroid shaped central housing machined from aluminum, and two aluminum side plates. To avoid entanglement with any object found inside the mine tunnels, two manifold systems, fixed to the side plates, have been designed for thruster mounting and propulsion.

FIGURE 3. Exploded view of robot aluminum external hull and side plates for sealing the watertight hull and fixing manifolds.

2) PENDULUM AND VARIABLE BALLAST SYSTEMS

The robot is expected to have an operating time of more than 3 hours for mine surveying missions on a single charge of the batteries. This requires the mechanical design to limit the power consumption of the propulsion system as much as possible. Therefore, as can be seen in Fig. 4, a Pendulum System (PS), for passive pitch stabilization, and a Variable Ballast System (VBS), for buoyancy control, have been integrated inside the watertight hull [19].

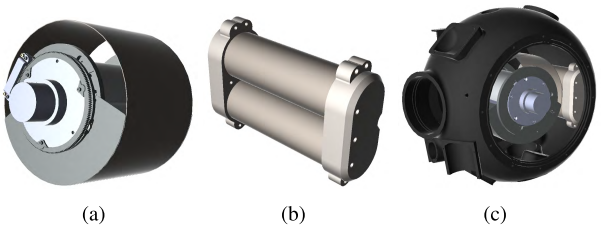

FIGURE 4. (a) Pendulum, (b) variable ballast systems, and (c) installation of systems in the hull.

B. HARDWARE & SENSORS

1) ON-BOARD COMPUTING

The robot has a distributed computer system for on-board data processing, sensor interfaces and actuator control [20]. Given the size restrictions inside the hull, a Com Express Type 6 (i7-8850H processor at 2.6/4.3GHz with QM370 chipset) PC was chosen as the main computer in charge of mission control. This computer hosts the Guidance, Navigation and Control (GNC) algorithms, as well as data fusion algorithms and hardware drivers and interfaces.

2) SENSOR COMMUNICATIONS

Sensors in the robot communicate to the main computer through Ethernet, RS485/422 or CAN Bus interfaces [20]. Low bandwidth components, such as the energy management system and actuator controls (thrusters, PS and VBS) use either serial or CAN interfaces. The thruster speed and VBS components are controlled by VESC (http://vedder.se/) Electronic Speed Controllers and communicate using CAN Bus.

3) PERCEPTION SUBSYSTEM

The perception subsystem of the includes a Konsberg M3 Multibeam Sonar (www.km.kongsberg.com), five digital cameras and rotating laser line projectors for structured light systems. These perception components are exploited to gather 3D map data during dive missions for use in navigation and post-processing tasks.

4) LOCALIZATION SUBSYSTEM

The UX-1 is equipped with a KVH 1750 (www.kvh.com) fiber optic Inertial Measurement Unit (IMU) for feedback of linear accelerations and angular velocities, as well as a Doppler Velocity Logger (DVL) for feedback of linear velocities and distance to bottom measurements. These measurements are used by an Extended Kalman Filter (EKF) to estimate the pose of the robot during missions.

III. DYNAMIC MODEL

The equations of motion for underwater vehicles have been extensively studied and presented in previous works, such as [21]. The vehicle is modeled as a body moving freely in space, namely characterized by 6 DOF, and derived according to the Society of Naval Architects and Marine Engineers (SNAME) notation [22].

A. NOMENCLATURE

Given that the purpose of the robot is to conduct autonomous underwater navigation, without the need for human intervention, two reference frames are adopted.

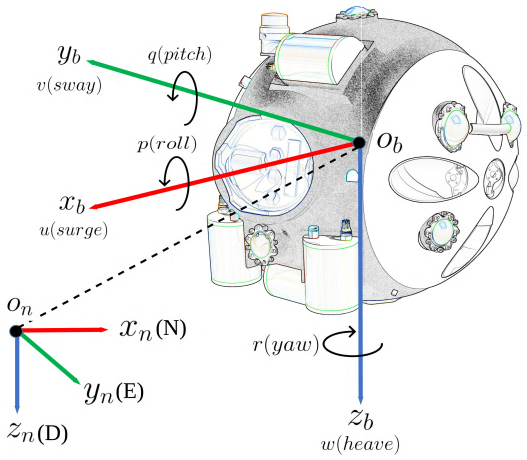

FIGURE 5. Schematics of the developed underwater vehicle with the reference frames used in the equations of motion.

As can be seen in Fig. 5, a North-East-Down (NED) reference frame $\{n\}$ is used, with orthonormal basis $\{x_n, y_n, z_n\}$ and origin o_n represented in world coordinates, where, for vehicles operating in a local area with approximately constant latitude and longitude, the NED reference frame can be considered inertial [21]. Additionally, a body-fixed reference frame $\{b\}$ is used with orthonormal basis $\{x_b, y_b, z_b\}$ and origin o_b also in world coordinates. The equations of motion presented in this work make use of the representation presented in [21], i.e.:

$$\boldsymbol{\eta} = \begin{bmatrix} \boldsymbol{P}^n_{b/n} \\ \boldsymbol{\Theta}_{nb} \end{bmatrix} = [x, y, z, \phi, \theta, \psi]^\top \tag{1}$$

$$\boldsymbol{J}_{\boldsymbol{\Theta}}(\boldsymbol{\eta}) = \begin{bmatrix} \boldsymbol{R}^n_b(\boldsymbol{\Theta}_{nb}) & \boldsymbol{0}_{3\times3} \\ \boldsymbol{0}_{3\times3} & \boldsymbol{T}_\Theta(\boldsymbol{\Theta}_{nb}) \end{bmatrix} \tag{2}$$

$$\boldsymbol{\nu} = \begin{bmatrix} \boldsymbol{v}^b_{b/n} \\ \boldsymbol{\omega}^b_{b/n} \end{bmatrix} = [u, v, w, p, q, r]^\top \tag{3}$$

$$\boldsymbol{\tau} = \begin{bmatrix} \boldsymbol{f}^b_b \\ \boldsymbol{m}^b_b \end{bmatrix} = [X, Y, Z, K, M, N]^\top \tag{4}$$

where $\boldsymbol{\eta} \in \mathbb{R}^3 \times \mathcal{S}^3$ denotes the position and orientation vector in the NED coordinate system. In (1), the position vector $\boldsymbol{P}^n_{b/n} \in \mathbb{R}^3$ is defined as the distance of point o_b with respect to $\{n\}$ expressed in $\{n\}$ and $\boldsymbol{\Theta}_{nb} \in \mathcal{S}^3$ is a vector of Euler angles, i.e., roll, pitch and yaw angles, denoted with ϕ, θ and ψ between $\{n\}$ and $\{b\}$. $\boldsymbol{J}_{\boldsymbol{\Theta}}(\boldsymbol{\eta})$ is a 6×6 Jacobian matrix consisting of a rotation matrix $\boldsymbol{R}^n_b(\boldsymbol{\Theta}_{nb})$, for transforming linear velocities in $\{b\}$ to $\{n\}$, and a transformation matrix $\boldsymbol{T}_\Theta(\boldsymbol{\Theta}_{nb})$ to relate the angular velocities $\boldsymbol{\omega}^b_{b/n}$ in $\{b\}$ to the Euler rate vector $\dot{\boldsymbol{\Theta}}_{nb}$. In (3), $\boldsymbol{\nu} \in \mathbb{R}^6$ denotes the linear $\boldsymbol{v}^b_{b/n}$ and angular $\boldsymbol{\omega}^b_{b/n}$ velocity vectors in the body-fixed reference frame, and in (4), $\boldsymbol{\tau} \in \mathbb{R}^6$ is used to describe the forces $\boldsymbol{f}^b_b$ and moments $\boldsymbol{m}^b_b$ acting on the vehicle in the body-fixed reference frame.

B. NONLINEAR 6 DOF MODEL

The nonlinear equations of motion for an UUV, as developed in [23], are:

$$\dot{\boldsymbol{\eta}} = \boldsymbol{J}_{\boldsymbol{\Theta}}(\boldsymbol{\eta})\boldsymbol{\nu} \tag{5}$$

$$\boldsymbol{M}\dot{\boldsymbol{\nu}} + \boldsymbol{C}(\boldsymbol{\nu})\boldsymbol{\nu} + \boldsymbol{D}(\boldsymbol{\nu})\boldsymbol{\nu} + \mathrm{g}(\boldsymbol{\eta}) = \boldsymbol{B}\boldsymbol{\tau} \tag{6}$$

with:

$$\boldsymbol{M} = \boldsymbol{M}_{RB} + \boldsymbol{M}_A, \quad \boldsymbol{M} = \boldsymbol{M}^\top > 0 \tag{7}$$

$$\boldsymbol{C}(\boldsymbol{\nu}) = \boldsymbol{C}_{RB}(\nu) + \boldsymbol{C}_A(\nu) \tag{8}$$

$$\boldsymbol{D}(\boldsymbol{\nu}) = \boldsymbol{D} + \boldsymbol{D}_n(\boldsymbol{\nu}) \tag{9}$$

where $\boldsymbol{B}$ is used as a mapping matrix for thruster configuration, and $\mathrm{g}(\boldsymbol{\eta})$ is the vector of hydrostatic forces and moments for the gravitational and buoyant forces acting on the vehicle. The system inertia matrix $\boldsymbol{M}$ is a positive semi-definite matrix composed of the rigid-body inertia matrix $\boldsymbol{M}_{RB}$, and the hydrodynamic inertia matrix of added mass terms $\boldsymbol{M}_A$. The Coriolis and Centripetal term matrix $\boldsymbol{C}(\boldsymbol{\nu})$, consists of the rigid-body $\boldsymbol{C}_{RB}(\nu)$, and hydrodynamic $\boldsymbol{C}_A(\nu)$ Coriolis and Centripetal matrices. Lastly, the total hydrodynamic damping matrix $\boldsymbol{D}(\boldsymbol{\nu})$ is the sum of the linear term $\boldsymbol{D}$, and the nonlinear term $\boldsymbol{D}_n(\boldsymbol{\nu})$.

C. RIGID-BODY FORCES

The rigid-body equations of motion are based on the rigid-body inertia matrix $\boldsymbol{M}_{RB}$ and the rigid-body Coriolis and Centripetal matrix $\boldsymbol{C}_{RB}(\nu)$.

1) RIGID-BODY INERTIA MATRIX

The representation of the rigid-body system inertia matrix in (7) is defined by:

$$\boldsymbol{M}_{RB} = \begin{bmatrix} m & 0 & 0 & 0 & mz_g & -my_g \\ 0 & m & 0 & -mz_g & 0 & mx_g \\ 0 & 0 & m & my_g & -mx_g & 0 \\ 0 & -mz_g & my_g & I_x & -I_{xy} & -I_{xz} \\ mz_g & 0 & -mx_g & -I_{yx} & I_y & -I_{yz} \\ -my_g & mx_g & 0 & -I_{zx} & -I_{zy} & I_z \end{bmatrix} \tag{10}$$

which satisfies, $\boldsymbol{M}_{RB} = \boldsymbol{M}_{RB}^{\top} > 0$ and $\dot{\boldsymbol{M}}_{RB} = \boldsymbol{0}_{6\times 6}$. In (10), m is the mass of the vehicle, $\{I_x, I_y, I_z\}$ are the moments of inertia about $\{b\}$ axes, $\{I_{xy} = I_{yx}, I_{xz} = I_{zx}, I_{yz} = I_{zy}\}$ are the products of inertia as defined in [21], and $\{x_g, y_g, z_g\}$ are the distances from the geometrical center of the vehicle to the center of gravity (CG). For the case of a spherical UUV with symmetry in the xz, yz and xy planes, the rigid-body inertia matrix can be approximated by:

$$\boldsymbol{M}_{RB} \approx diag\{m, m, m, I_x, I_y, I_z\}. \tag{11}$$

2) RIGID-BODY CORIOLIS AND CENTRIPETAL MATRIX

The rigid-body Coriolis and Centripetal matrix $\boldsymbol{C}_{RB}(\nu)$ terms are due to a rotation of the body-fixed reference frame $\{b\}$ about the inertial frame $\{n\}$. According to [23], $\boldsymbol{C}_{RB}(\nu)$ can always be represented such that it is skew-symmetric (i.e., $\boldsymbol{C}_{RB}(\nu) = -\boldsymbol{C}_{RB}^{\top}(\nu)$) and defined as:

$$\boldsymbol{C}_{RB}(\boldsymbol{\nu}) = \begin{bmatrix} 0 & 0 & 0 & mz_g r & mw & -mv \\ 0 & 0 & 0 & -mw & mz_g r & mu \\ 0 & 0 & 0 & -m\alpha_1 & -m\alpha_2 & 0 \\ -mz_g r & mw & m\alpha_1 & 0 & I_z r & -I_y q \\ -mw & -mz_g r & m\alpha_2 & -I_z r & 0 & I_x p \\ mv & -mu & 0 & I_y q & -I_x p & 0 \end{bmatrix} \tag{12}$$

with

$$\alpha_1 = (z_g p - v), \quad \alpha_2 = (z_g q + u). \tag{13}$$

D. HYDRODYNAMIC FORCES

In this section the hydrodynamic forces acting on the UUV are presented. These are: the added mass forces, the hydrodynamic inertia matrix of added mass terms $\boldsymbol{M}_A$, the hydrodynamic Coriolis and Centripetal matrix $\boldsymbol{C}_A(\boldsymbol{\nu})$, and the hydrodynamic damping matrix $\boldsymbol{D}(\boldsymbol{\nu})$.

1) HYDRODYNAMIC ADDED MASS FORCES

Added mass forces arise due to the exchange of inertia among a moving object and its surrounding fluid. This force can be described by an axial component and a rolling component. Assuming that the shape of the UUV can be approximated by an ellipsoid, the axial component of the hydrodynamic added mass force X along the x axis due to an acceleration $\dot{u}$ in the x direction is computed as [24]:

$$X_{\dot{u}} = \frac{4\,\beta\,\rho\,\pi}{3}\left(\frac{d}{2}\right)^3 \tag{14}$$

where $X_{\dot{u}}$ is known as a hydrodynamic derivative according to the SNAME notation, ρ is the water density, d is the diameter of the vehicle, and β is a coefficient based on the ratio between the vehicle length and diameter. Similar considerations hold for the axial components of the hydrodynamic added mass force, Y and Z.

The authors in [25] provide the following expression to compute the rolling component of the hydrodynamic added mass force for a prolate spheroid:

$$K_{\dot{p}} = \frac{4}{15}\,\pi\,\rho\,a\,b^2\,(a^2 + b^2) \tag{15}$$

where a and b represent the two semi-axis of the spheroid. For the special case of a spherical UUV, the three rolling components of the hydrodynamic added mass force are all equal, i.e. $K_{\dot{p}} = M_{\dot{q}} = N_{\dot{r}}$. Furthermore, the non-idealities, namely the external sensors and actuators, can be accounted for using the expression provided in [26], under the assumption of considering them as fins:

$$K_{\dot{p}_f} = -\sum_{i=1}^{n_{fins}} \int_{x_{init_i}}^{x_{end_i}} \frac{2}{\pi}\,\rho\,r_i^4\,dx \tag{16}$$

where r_i is the i-th fin height above the vehicle centerline, x_{init_i} is the starting point of the i-th fin, x_{end_i} is the ending point of the i-th fin, and n_{fins} is the number of fins.

2) HYDRODYNAMIC SYSTEM INERTIA MATRIX

The system inertia matrix of added mass terms $\boldsymbol{M}_A$ describes the mass that the UUV has to displace while moving, and the inertia due to the displaced mass while rotating. Since the equations of motion of an UUV moving at high speeds are highly nonlinear and coupled, in this work the vehicle is restricted to perform low speed maneuvers only. Therefore, for the case of a spherical UUV with three planes of symmetry, the contribution of the off-diagonal elements in the added mass inertia matrix can be neglected. Hence,

$$\boldsymbol{M}_A = \boldsymbol{M}_A^{\top} = -diag\{X_{\dot{u}}, Y_{\dot{v}}, Z_{\dot{w}}, K_{\dot{p}}, M_{\dot{q}}, N_{\dot{r}}\} \tag{17}$$

The added mass matrix elements $X_{\dot{u}}$, $Y_{\dot{v}}$, $Z_{\dot{w}}$, $K_{\dot{p}}$, $M_{\dot{q}}$ and $N_{\dot{r}}$ are the hydrodynamic added mass forces as explained in Section III-D1.

3) HYDRODYNAMIC CORIOLIS AND CENTRIPETAL MATRIX

The nonlinear hydrodynamic Coriolis and Centripetal matrix $\boldsymbol{C}_A(\boldsymbol{\nu})$ can be derived using an energy formulation based on

the added mass matrix (17) [27], as follows:

$$\boldsymbol{C}_A(\boldsymbol{\nu}) = \begin{bmatrix} 0 & 0 & 0 & 0 & -Z_{\dot{w}}w & Y_{\dot{v}}v \\ 0 & 0 & 0 & Z_{\dot{w}}w & 0 & -X_{\dot{u}}u \\ 0 & 0 & 0 & -Y_{\dot{v}}v & X_{\dot{u}}u & 0 \\ 0 & -Z_{\dot{w}}w & Y_{\dot{v}}v & 0 & -N_{\dot{r}}r & M_{\dot{q}}q \\ Z_{\dot{w}}w & 0 & -X_{\dot{u}}u & N_{\dot{r}}r & 0 & -K_{\dot{p}}p \\ -Y_{\dot{v}}v & X_{\dot{u}}u & 0 & -M_{\dot{q}}q & K_{\dot{p}}p & 0 \end{bmatrix} \tag{18}$$

4) HYDRODYNAMIC DAMPING MATRIX

The hydrodynamic damping of an underwater vehicle can be modeled as the sum of two concentrated forces, lift and drag. The lift force arises from the difference of pressure generated by fluid flowing over the upper and lower parts of the hull, further depending on the angle of attack and on the speed of the vehicle. For a spherical UUV, the pressure difference is assumed null and the lift force is neglected.

The drag force of an underwater vehicle operating in a closed space mainly depends on linear-skin friction and cavitation. For a low-speed moving vehicle, the drag can be considered decoupled among the DOF. This force can be expressed with two formulations, one arising when the vehicle performs a motion along an axis, named axial and cross flow drag, and another when the vehicle rotates around an axis, referred to as rolling drag. The axial drag term is the drag force directed towards the x axis of the UUV and it is often expressed as a quadratic function of speed, using the following formulation:

$$X_{|u|u} = \frac{1}{2}\,\rho\, C_d(Re)\, A \tag{19}$$

where A is the vehicle cross sectional area and $C_d(Re)$ is the drag coefficient which depends on the Reynolds number (Re). The crossflow drag terms affect the vehicle when moving perpendicular to it's x axis, i.e. heave and sway motions. For a spherical UUV, the crossflow drag can be calculated using:

$$Y_{|v|v} = Z_{|w|w} = -\frac{1}{2}\rho C_d A - \sum_{i=1}^{n_{fin}} \left(\frac{1}{2}\rho S_{fin,i} C_{d_{fin,i}}\right) \tag{20}$$

where S_{fin_i} is the surface of the i-th fin, $C_{d_{fin,i}}$ is the drag coefficient of the i-th fin, and n_{fin} denotes the number of fins. Assuming that the external sensors can be considered as fins, the drag coefficient of each sensor can be computed using the fin taper ratio approximation t_i:

$$C_{d_{fin_i}} = 0.1 + 0.7 t_i \tag{21}$$

where

$$t_i = \frac{width\ on\ top_i}{width\ on\ bottom_i}. \tag{22}$$

A perfect rolling sphere produces an extremely low drag [26]. The main component of the rolling drag is thus generated by fins, and the following approximated expression can be used:

$$K_{|p|p} = Y_{|v|v}\, r_{mean}^3 \tag{23}$$

where r_{mean} is the mean fin (or external sensor) height above the vehicle axis centerline. Similar formulations can be used to calculate $M_{|q|q}$ and $N_{|r|r}$ Thus, the hydrodynamic damping matrix $\boldsymbol{D}(\boldsymbol{\nu})$ can be expressed as [23]:

$$\begin{aligned} \boldsymbol{D}(\boldsymbol{\nu}) = & -diag\{X_u, Y_v, Z_w, K_p, M_q, N_r\} \\ & - diag\{X_{|u|u}|u|, Y_{|v|v}|v|, Z_{|w|w}|w|, \\ & K_{|p|p}|p|, M_{|q|q}|q|, N_{|r|r}|r|\} \end{aligned} \tag{24}$$

where $\{X_u, Y_v, Z_w, K_p, M_q, N_r\}$ are the linear damping term $\boldsymbol{D}$ coefficients using the SNAME notation. Definitions and theory can be found in [28].

E. HYDROSTATIC FORCES

Conforming to the SNAME nomenclature, the weight W and buoyancy B of a submerged vehicle are given by,

$$W = mg, \quad B = \rho g \nabla \tag{25}$$

where g is the Earth's gravitational constant in NED and ∇ is the volume of the displaced water mass, i.e., volume of the vehicle. Since these forces only affect the vertical plane of $\{n\}$, they can be expressed as [29]:

$$\boldsymbol{f}_g^n = \begin{bmatrix} 0 & 0 & W \end{bmatrix}^\intercal \qquad \boldsymbol{f}_b^n = \begin{bmatrix} 0 & 0 & -B \end{bmatrix}^\intercal \tag{26}$$

These forces are expressed in the inertial frame $\{n\}$, thus, they can be moved to the body-fixed frame $\{b\}$ by applying the coordinate transformation matrix $\boldsymbol{R}_b^n(\boldsymbol{\Theta}_{nb})$. Once rotated to $\{b\}$, (26) can be rewritten as:

$$\mathrm{g}(\boldsymbol{\eta}) = -\begin{bmatrix} \boldsymbol{f}_g^b + \boldsymbol{f}_b^b \\ \boldsymbol{r}_g^b \times \boldsymbol{f}_g^b + \boldsymbol{r}_b^b \times \boldsymbol{f}_b^b \end{bmatrix} \tag{27}$$

where $\boldsymbol{r}_g^b$ and $\boldsymbol{r}_b^b$ are the vectors collecting the distances from the body-fixed frame to the centers of application of the forces, i.e., they represent the distances from the geometrical center of the sphere to the CG and the Center of Buoyancy (CB), respectively. Hence, expanding (27), the vector collecting the effect of the hydrostatic forces and moments, namely $\mathrm{g}(\boldsymbol{\eta})$, is as follows:

$$\mathrm{g}(\boldsymbol{\eta}) = \begin{bmatrix} (W-B)s\theta \\ -(W-B)c\theta s\phi \\ -(W-B)c\theta c\phi \\ -(y_g W - y_b B)c\theta c\phi + (z_g W - z_b B)c\theta s\phi \\ (x_g W - x_b B)c\theta c\phi + (z_g W - z_b B)s\theta \\ (x_g W - x_b B)c\theta s\phi - (y_g W - y_b B)s\theta \end{bmatrix} \tag{28}$$

where $s(\cdot) = \sin(\cdot)$ and $c(\cdot) = \cos(\cdot)$. As can be seen in (28), if the UUV is close to neutrally buoyant ($W = B$), the gravitational forces only affect the rotations in the x and y axes.

F. QUATERNION REPRESENTATION

In the previous sections, any rotation from the inertial frame $\{n\}$ to the body-fixed frame $\{b\}$ or viceversa is performed by means of the transformation matrix $\boldsymbol{J}_{\boldsymbol{\Theta}}(\boldsymbol{\eta})$ in (2), that includes the following matrices:

$$\boldsymbol{R}_b^n(\boldsymbol{\Theta}_{nb}) = \begin{bmatrix} c\psi c\theta & -s\psi c\phi + c\psi s\theta s\phi & s\psi s\phi + c\psi c\phi s\theta \\ s\psi c\theta & c\psi c\phi + s\psi s\theta s\phi & -c\psi s\phi + s\psi c\phi s\theta \\ -s\theta & c\theta s\phi & c\theta c\phi \end{bmatrix}, \tag{29}$$

$$\boldsymbol{T}_{\Theta}(\boldsymbol{\Theta}_{nb}) = \begin{bmatrix} 1 & 0 & -s\theta \\ 0 & c\phi & c\theta s\phi \\ 0 & -s\phi & c\theta c\phi \end{bmatrix}. \tag{30}$$

This transformation is achieved by means of three sequential rotations around three axes. If the rotations are performed starting from one axis of the inertial frame, Euler angles can be used to express the attitude of the body-fixed frame. This approach is commonly used in robotic applications since the kinematic parameters preserve the physical meaning of the attitude of the vehicle and the approach can be applied for any attitude, except for the singularity in a pitch angle θ of $\pm 90°$.

Nevertheless, in the case of UX-1, the configuration with the critical pitch angle $\pm 90°$ is a standard working condition, corresponding to the maneuver of ascending or descending in a mine shaft. In order to allow for a complete range of motions, the following quaternion parameterization is used as well:

$$\boldsymbol{J}_{\boldsymbol{q}}(\boldsymbol{\eta}) = \begin{bmatrix} \boldsymbol{R}_b^n(\boldsymbol{q}) & \boldsymbol{0}_{3\times 3} \\ \boldsymbol{0}_{4\times 3} & \boldsymbol{T}_q(\boldsymbol{q}) \end{bmatrix} \tag{31}$$

with

$$\boldsymbol{R}_b^n(q) = \begin{bmatrix} 1-2(q_2^2+q_3^2) & 2(q_1\,q_2 - q_3\,q_0) & 2(q_1\,q_3 - q_2\,q_0) \\ 2(q_1\,q_2 + q_3\,q_0) & 1-2(q_1^2+q_3^2) & 2(q_2\,q_3 - q_1\,q_0) \\ 2(q_1\,q_3 - q_2\,q_0) & 2(q_2\,q_3 + q_1\,q_0) & 1-2(q_1^2+q_2^2) \end{bmatrix} \tag{32}$$

$$\boldsymbol{T}_q(\boldsymbol{q}) = \frac{1}{2}\begin{bmatrix} -q_1 & -q_2 & -q_3 \\ q_0 & -q_3 & q_2 \\ q_3 & q_0 & -q_1 \\ -q_2 & q_1 & q_0 \end{bmatrix} \tag{33}$$

The notation used for the quaternions is the following, $[q_0\ q_1\ q_2\ q_3]$, where q_0 denotes the scalar component of the unit quaternion. Additionally, the quaternion parameterization can be used to represent the vector of hydrostatic forces and moments in (28) as:

$$\mathrm{g}(\boldsymbol{\eta}) = \begin{bmatrix} 2q_c(W-B) \\ -2q_d(W-B) \\ q_b(W-B) \\ -q_b(y_g W - y_b B) - 2q_d(z_g W - z_b B) \\ -q_b(x_g W - x_b B) - 2q_c(z_g W - z_b B) \\ -2q_d(x_g W - x_b B) - 2q_c(y_g W - y_b B) \end{bmatrix} \tag{34}$$

where $q_b = -q_0^2 + q_1^2 + q_2^2 - q_3^2$, $q_c = q_0 q_2 - q_1 q_3$ and $q_d = q_0 q_1 + q_2 q_3$.

IV. UX-1 CONTROL SYSTEM

As it can be seen in Fig. 6, a modular control system, where control modules can be easily replaced for testing different control strategies, has been adopted for UX-1 robot.

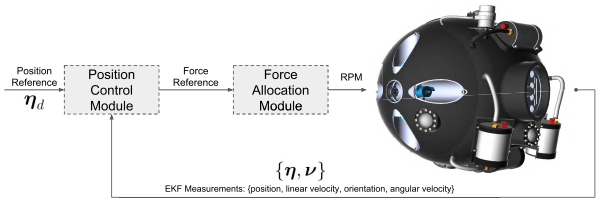

FIGURE 6. General position control scheme implemented on UX-1.

A force allocation module is first designed, in charge of interpreting the force requirements and distributing it to the actuators, followed by an outer position control module in charge of computing the reference force vector based on the desired position reference and the actual robot position. To design the position control module, different strategies are considered, starting from a multivariable linear optimal approach and then exploiting a nonlinear approach.

A. FORCE ALLOCATION MODULE

The UX-1 is an over-actuated system, where the number of actuators used to perform a control action is redundant, either to improve system performance, reliability or robustness [30]. The force allocation control approach is based on the mapping matrix, which gathers how the forces of the actuators generate effects on the control force vector of the system. The idea of this approach is that, given a reference force vector and inverting the mapping matrix, it is possible to compute the force required by each actuator.

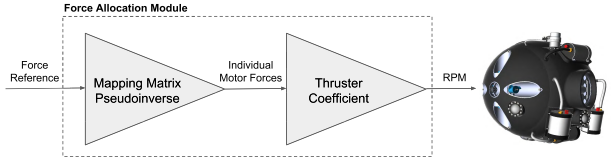

FIGURE 7. Components of force allocation module for UX-1.

1) MAPPING MATRIX

The mapping matrix $\boldsymbol{B}$, shown in (6), is used to define how the thruster configuration will act on the dynamics of the UUV. UX-1 is actuated by means of eight thrusters, hereby denoted $\{T_i\}$, allocated symmetrically on each side of the vehicle. Therefore, $\boldsymbol{B}$ will be a 6×8 matrix with the rows corresponding to the DOF, i.e. $\{X, Y, Z, K, M, N\}$, and the columns corresponding to each thruster, i.e. $\{T_1, \ldots, T_8\}$; where element i,j expresses how the $i-th$ DOF is affected by the $j-th$ thruster. For any given motion, several combinations

TABLE 1. Mapping matrix actuator configuration for UX-1.

Motion	Positive Movement	Negative Movement
Surge	$\{T_1, T_5\}$	$\{T_3, T_7\}$
Sway	$\{T_1, T_2, T_3, T_4\}$	$\{T_5, T_6, T_7, T_8\}$
Heave	$\{T_2, T_6\}$	$\{T_4, T_8\}$
Roll	$\{T_4, T_6\}$	$\{T_2, T_8\}$
Yaw	$\{T_1, T_7\}$	$\{T_3, T_5\}$

of thrusters can be chosen using the thruster notation shown in Fig. 2.

The configuration of actuators chosen for the different motions is shown in Table 1. Using this configuration, the mapping matrix $\boldsymbol{B}$ of the effect of the thrusters on the dynamics of the system is defined as:

$$\boldsymbol{B} = \begin{bmatrix} 1 & 0 & -1 & 0 & 1 & 0 & -1 & 0 \\ 1 & 1 & 1 & 1 & -1 & -1 & -1 & -1 \\ 0 & 1 & 0 & -1 & 0 & 1 & 0 & -1 \\ 0 & -l & 0 & l & 0 & l & 0 & -l \\ 0 & 0 & 0 & 0 & 0 & 0 & 0 & 0 \\ l & 0 & -l & 0 & -l & 0 & l & 0 \end{bmatrix} \tag{35}$$

with

$$l = \sin(\delta)\sqrt{{\sigma_1}^2 + {\sigma_2}^2} \tag{36}$$

where σ_1 is the distance from the axis of the thrusters to the geometrical center of the UUV, σ_2 is the distance from each thruster to the middle lateral point and $\delta = \arctan(\frac{\sigma_2}{\sigma_1})$ is the rotation angle of the moments generated on the UUV.

2) MAPPING MATRIX PSEUDOINVERSE

Since the mapping matrix $\boldsymbol{B}$ in (35) is not a square matrix, the pseudoinverse of $\boldsymbol{B}$, denoted with $\boldsymbol{B}^\dagger$, can be used to solve the problem. The pseudoinverse matrix is calculated using the *Moore-Penroose inverse* as:

$$\boldsymbol{B}^\dagger = (\boldsymbol{B}^\top \boldsymbol{B})^{-1} \boldsymbol{B}^\top. \tag{37}$$

3) THRUSTER COEFFICIENT

As can be seen in Fig. 7, the output of the mapping matrix pseudoinverse evaluated in the previous section is represented by the desired forces from each of the eight thrusters, i.e. $[F_{T_1}, F_{T_2}, \ldots, F_{T_8}]$. However, the input for the VESC Electronic Speed Controllers, used to control the speed of the thrusters, are the desired thruster velocities in RPM. To translate the desired force of each thruster F_{T_i} to a desired velocity, a simple relation is derived as:

$$F_{T_i} = k_m \omega_{T_i}^2 \tag{38}$$

where k_m is the thruster coefficient and $\omega_{T_i}^2$ is the speed of the $i-th$ thruster in RPM. This model neglects the dynamics of the thrusters and considers them as being capable of providing the required force instantaneously. This is a reasonable assumption, given that the maximum operating speed of the UX-1 robot during missions is around 0.5 m/s with minimum changes in attitude. Experimental tests that were performed to identify the characteristic curve of the thrusters will be shown in Section V-B1.

B. POSITION CONTROL MODULE

For the position control module, two methods are presented in this work. First, a Finite Horizon Linear Quadratic Regulator (LQR) which is based on two loops for speed and position control. Afterwards, a State Feedback Linearization control which is based on a single loop with position and velocity feedback.

1) FINITE HORIZON LQR

This method is based on a multivariable approach, chosen as the Linear Quadratic control (*LQ*). The *LQ* regulator solves the control problem by minimizing the performance index:

$$\boldsymbol{J} = \frac{1}{2}\int_0^\infty ((\boldsymbol{x} - \boldsymbol{x}_R)^\top \boldsymbol{Q}(\boldsymbol{x} - \boldsymbol{x}_R) + (\boldsymbol{u} - \boldsymbol{u}_R)^\top \boldsymbol{R}(\boldsymbol{u} - \boldsymbol{u}_R))\, dt \tag{39}$$

where $\boldsymbol{x}$ is the vector of the states, $\boldsymbol{x}_R$ is the vector of the state references, $\boldsymbol{u}$ is the vector of the inputs, $\boldsymbol{u}_R$ is the vector of input references and, $\boldsymbol{Q}$, $\boldsymbol{R}$ are the matrices of state and input weights, respectively.

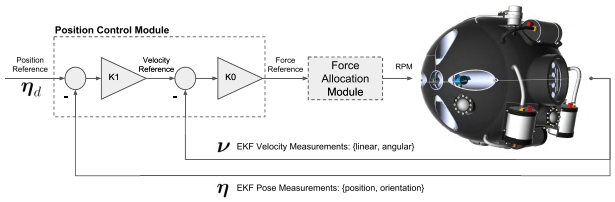

FIGURE 8. Linear quadratic regulator control architecture.

As shown in Fig. 8, the control is constituted by two nested loops, an inner one in charge of the velocity control and an outer targeting the position. The two control gains K_0 and K_1 are tuned solving two independent LQ problems. For the speed a linearized version of the dynamic equations in (6) has been used, whilst for the position a linearized kinematic model, derived from (5) is adopted.

The state gain matrix Q of the LQ controller are chosen according to [31], in which the state gain is designed as a diagonal matrix where each term on the main diagonal is normalized dividing by the square of the maximum acceptable error as follows,

$$q_i = \left(\frac{1}{max\ error_i}\right)^2. \tag{40}$$

The control weight R is a tuning parameter related to the energy consumption of the control strategy, with higher gains meaning a faster system at the cost of an higher energy requirement. R is tuned by dynamic simulations of the system, choosing a trade-off between response time and required control forces, and afterwards tuned in experimental tests.

2) NONLINEAR STATE FEEDBACK LINEARIZATION

The State Feedback Linearization (FL) control method has been implemented and validated in a number works in the literature. The main principle with feedback linearization is the transformation of the nonlinear dynamics of the UUV into a set of independent chain of integrators, as follows:

$$\ddot{\boldsymbol{\eta}} = \boldsymbol{\lambda}^n \tag{41}$$

$$\dot{\boldsymbol{\nu}} = \boldsymbol{\lambda}^b \tag{42}$$

to which traditional control methods for linear dynamical systems (e.g. Linear Quadratic Regulator, pole-placement) can be applied [21]. In (41), $\boldsymbol{\lambda}^n$ is interpreted as the commanded acceleration in the NED frame, and in (42) $\boldsymbol{\lambda}^b$ as the body-fixed commanded acceleration vector.

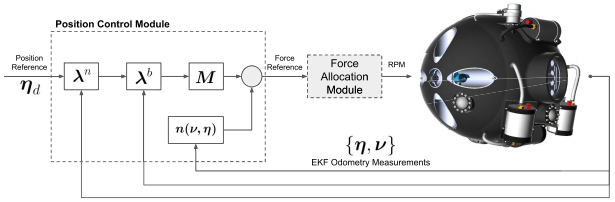

FIGURE 9. State feedback linearization controller architecture.

We consider the nonlinear kinematic and dynamic equations from Section III-B in the form

$$\dot{\boldsymbol{\eta}} = \boldsymbol{J}_{\boldsymbol{\Theta}}(\boldsymbol{\eta})\boldsymbol{\nu} \tag{43}$$

$$\boldsymbol{M}\dot{\boldsymbol{\nu}} + \boldsymbol{n}(\boldsymbol{\nu}, \boldsymbol{\eta}) = \boldsymbol{\tau} \tag{44}$$

where $\boldsymbol{\eta}$ and $\boldsymbol{\nu}$ are assumed to be measurable and $\boldsymbol{n}$ is defined as follows,

$$\boldsymbol{n}(\boldsymbol{\nu}, \boldsymbol{\eta}) = \boldsymbol{C}(\boldsymbol{\nu})\boldsymbol{\nu} + \boldsymbol{D}(\boldsymbol{\nu})\boldsymbol{\nu} + \boldsymbol{g}(\boldsymbol{\eta}). \tag{45}$$

The control law is selected such that the nonlinearities of the system dynamics can be canceled out

$$\boldsymbol{\tau} = \boldsymbol{M}\boldsymbol{\lambda}^b + \boldsymbol{n}(\boldsymbol{\nu}, \boldsymbol{\eta}). \tag{46}$$

Differentiating (43) with respect to time and applying the control law (46) to the UUV dynamics in (44) yields

$$\boldsymbol{M}(\dot{\boldsymbol{\nu}} - \boldsymbol{\lambda}^b) = \boldsymbol{M}\boldsymbol{J}_{\boldsymbol{\Theta}}^{-1}(\boldsymbol{\eta})[\ddot{\boldsymbol{\eta}} - \dot{\boldsymbol{J}}_{\boldsymbol{\Theta}}(\boldsymbol{\eta})\boldsymbol{\nu} - \boldsymbol{J}_{\boldsymbol{\Theta}}(\boldsymbol{\eta})\boldsymbol{\lambda}^b] = \boldsymbol{0}. \tag{47}$$

Selecting

$$\boldsymbol{\lambda}^n = \dot{\boldsymbol{J}}_{\boldsymbol{\Theta}}(\boldsymbol{\eta})\boldsymbol{\nu} + \boldsymbol{J}_{\boldsymbol{\Theta}}(\boldsymbol{\eta})\boldsymbol{\lambda}^b \tag{48}$$

results in the linear decoupled system $\boldsymbol{M}^*(\ddot{\boldsymbol{\eta}} - \boldsymbol{\lambda}^n) \mathcal{D} \boldsymbol{0}$ where $\boldsymbol{M}^* = \boldsymbol{J}_{\boldsymbol{\Theta}}^{-\mathsf{T}}(\boldsymbol{\eta})\boldsymbol{M}\boldsymbol{J}_{\boldsymbol{\Theta}}^{-1}(\boldsymbol{\eta}) > 0$ (note that $J_\Theta(\eta)$ is a square matrix and it is always invertible). From (48) it can be concluded that the commanded acceleration in the body-fixed frame $\boldsymbol{\lambda}^b$ can be calculated by

$$\boldsymbol{\lambda}^b = \boldsymbol{J}_{\boldsymbol{\Theta}}^{-1}(\boldsymbol{\eta})[\boldsymbol{\lambda}^n - \dot{\boldsymbol{J}}_{\boldsymbol{\Theta}}(\boldsymbol{\eta})\boldsymbol{\nu}] \tag{49}$$

and the commanded acceleration in the NED frame can be chosen as a PD control law with acceleration feedforward

$$\boldsymbol{\lambda}^n = \ddot{\boldsymbol{\eta}}_d - \boldsymbol{K}_d\dot{\tilde{\boldsymbol{\eta}}} - \boldsymbol{K}_p\tilde{\boldsymbol{\eta}} \tag{50}$$

where $\boldsymbol{\eta}_d$ is the desired position and orientation vector in NED, $\tilde{\boldsymbol{\eta}} = \boldsymbol{\eta} - \boldsymbol{\eta}_d$ is the position and orientation tracking error and, $\boldsymbol{K}_p$ and $\boldsymbol{K}_d$ are positive definite diagonal matrices of the controller gains. These gains can be selected in order to set the desired error dynamics. In fact, introducing (50) in (41) we obtain the error dynamics $\ddot{\tilde{\boldsymbol{\eta}}} + \boldsymbol{K}_d\dot{\tilde{\boldsymbol{\eta}}} + \boldsymbol{K}_p\tilde{\boldsymbol{\eta}} = 0$.

V. EXPERIMENTS

Experimental tests were carried out to evaluate and compare the performance of the position control systems (Section IV). Furthermore, identification tests were performed in order to validate the theoretical hydrodynamic damping parameters for surge and pitch obtained from the derivation of the system model, and to calculate the thruster coefficient. The analysis of these experiments will be discussed in Section VI.

A. EXPERIMENTAL SETUP

To test the UX-1 robot in a underwater environment, a 10m × 6m × 5m depth test tank located in the Robotics and Autonomous Systems Laboratory at INESC TEC was used (Fig. 10). Using the measurements from the DVL and the IMU sensors installed on-board, an EKF algorithm developed by researchers at INESC TEC was used to estimate the UX-1 robot position and velocity feedback.

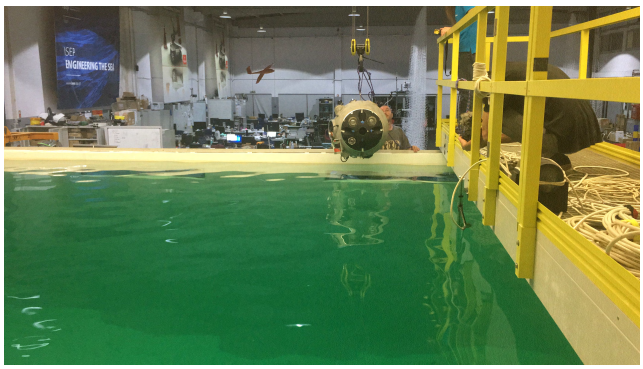

FIGURE 10. UX-1 robot entering water tank used for experimental tests.

All hardware interfaces have been implemented in Python or C++ in Ubuntu 16.04, and data communications are handled using the ROS (https://www.ros.org/) middleware standard messages. The UX-1 robot was designed and intended for fully autonomous navigation of flooded mines; however, during this phase of preliminary tests, the UX-1 robot was equipped with a neutrally buoyant tether for real-time controller tuning and manual control in case of controller failure.

The PS control has not been considered in this work; thus, the passive pitch stabilization was used to fix the pitch of the UX-1 to 0° during the underwater tests. Additionally, the VBS used for buoyancy control and trimming was not fully functional during these tests; therefore, the robot was trimmed with dead weights on the inside to get as close to neutral as possible.

B. MODEL PARAMETER IDENTIFICATION

1) THRUSTER COEFFICIENT IDENTIFICATION

To identify the thruster coefficient k_m in (38), an experimental test was performed using one of the UX-1 thrusters, a model T200 from BlueRobotics (www.bluerobotics.com). The motor was fixed to a metal rod connected to a load cell and secured to the test tank support bridge, as shown in Fig. 11.

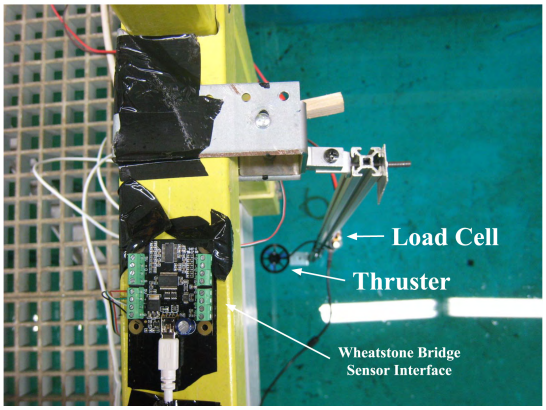

FIGURE 11. Motor parameter identification test setup.

First, the load cell was calibrated by incrementally adding known weights to the metal rod and measuring the correspondent output voltage. From the datasheet of the load cell, the relation from voltage to the corresponding force can be approximated with a linear curve as in Fig. 12.

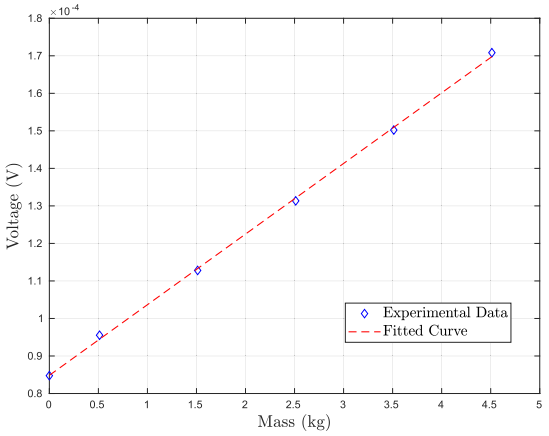

FIGURE 12. Load cell characteristic curve.

Once the characteristic coefficient of the load cell was computed, the force generated by the motor can be measured. The identification procedure was as follows:

- the motor is actuated within a known range of RPM values by means of the open-source *BLDC Tool*;
- for each RPM input a transient time is needed for the motor to reach the steady-state and for the test bench to exhaust any physical vibration;
- each RPM command is provided 20 times and their corresponding voltage measurements are averaged;
- the characteristic curve of the thruster is identified fitting the data to a quadratic model.

As expected from (38) and shown in Fig. 13, the data obtained from the identification tests are in good accordance with the expected quadratic model.

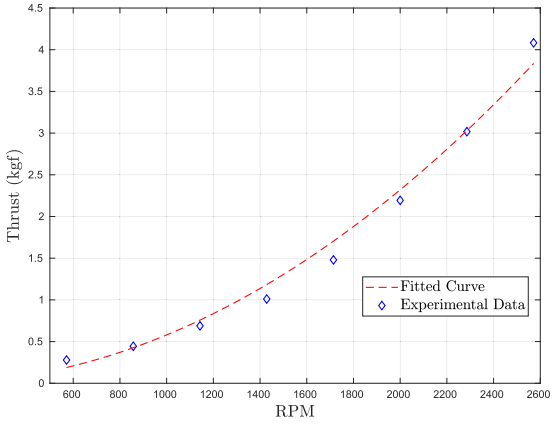

FIGURE 13. UX-1 thruster characteristic curve.

2) DAMPING PARAMETER IDENTIFICATION

Once the thruster coefficient was identified, the experimental identification test of the surge linear and quadratic damping terms, represented by $X_{|u|u}$ and X_u in (24), was performed. Two models have been considered for the surge motion, assumed to be decoupled from the other dynamics:

$$m\dot{u} = X_{|u|u}u|u| + X_{\dot{u}}\dot{u} + X_c \tag{51}$$

$$m\dot{u} = X_{|u|u}u|u| + X_u u + X_{\dot{u}}\dot{u} + X_c \tag{52}$$

where in (51) only the quadratic term of the drag $X_{|u|u}$ is accounted for, whereas in (52), both the linear X_u and quadratic $X_{|u|u}$ terms are considered. To identify the drag coefficients a test has been performed providing as input to the system a known linear force by means of the available thrusters, and measuring the resulting velocity of the vehicle from the DVL. The results of these experiments, together with the two identified models, are shown in Fig. 14.

3) ROLLING DRAG IDENTIFICATION

Lastly, the rolling drag coefficient for pitch, as described by $M_{|q|q}$ and M_q in (24), was experimentally identified. In order to measure the pitch angle, an underwater camera has been used. Two circular markers were positioned on one of the manifolds of the vehicle, as shown in Fig. 15, and an image processing algorithm based on Hough transform segmentation was developed to compute the pitch angle θ, using the following relation:

$$\theta = \arctan \frac{y_c - y_m}{x_c - x_m} \tag{53}$$

where $\{x_m, y_m\}$ are the coordinates of the center of the marker, and $\{x_c, y_c\}$ are the coordinates of the center of the vehicle.

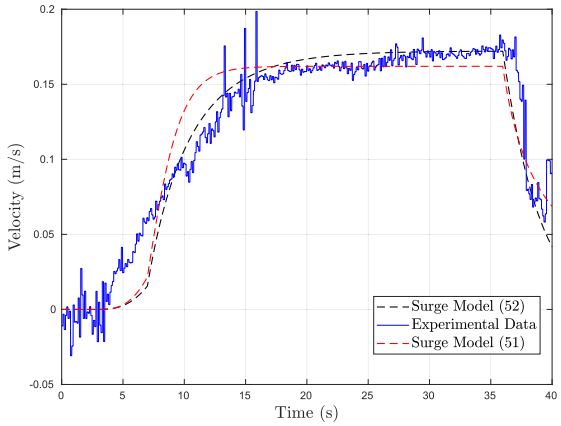

FIGURE 14. Linear drag identification results (blue line represents experimental data, red dashed line model (51), black dashed line model (52).

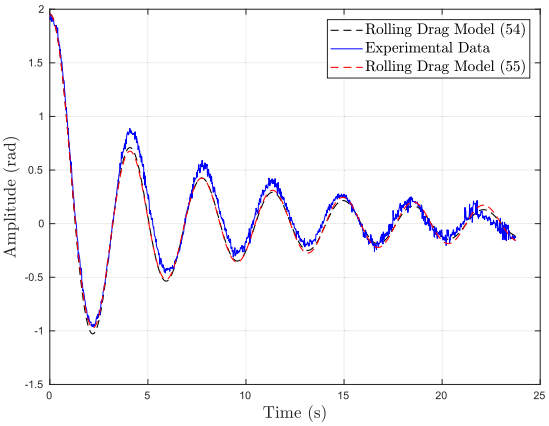

FIGURE 16. Rolling drag identification results (blue line represents experimental data, black dashed line model (54), red dashed line model (55).

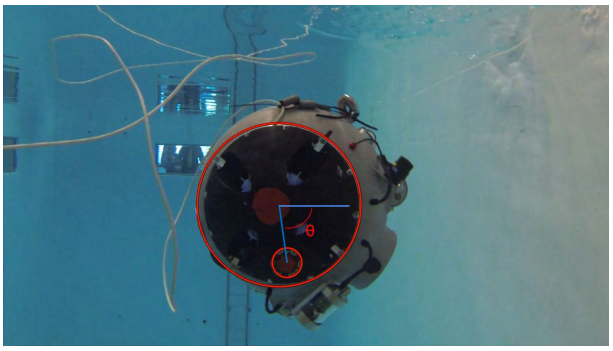

FIGURE 15. UX-1 during parameter identification experiments.

Again, two models of increasing complexity have been used,

$$I_{yy}\ddot{\theta} = z_g W \sin(\theta) + M_{|q|q}\dot{\theta}|\dot{\theta}| + M_{\dot{q}}\ddot{\theta} \tag{54}$$

$$I_{yy}\ddot{\theta} = z_g W \sin(\theta) + M_q\dot{\theta} + M_{|q|q}\dot{\theta}|\dot{\theta}| + M_{\dot{q}}\ddot{\theta}. \tag{55}$$

in (54) only the quadratic drag term $M_{|q|q}$ is considered, whereas in (55) the analysis is extended also to the linear term M_q. The rolling drag test is performed by imposing an initial step, manually pitching the vehicle upwards, and then computing in each frame the pitch angle geometrically from the markers. In Fig. 16, the fitting for both identified rolling drag models is presented.

C. UNDERWATER CONTROL TESTS

The underwater path tracking experiments were designed to simulate the UX-1 robot navigating inside an underwater mine tunnel environment. Position reference commands were sent in North (surge) and Depth (heave), while maintaining the East (sway) at $y = 0$m and the Heading (yaw) and roll fixed at 0°. As mentioned before, the PS for pitch control was fixed as to navigate in a nose forward configuration ($\phi = 0°$).

1) PATH TRACKING FEEDBACK LINEARIZATION CONTROL

The state feedback linearization control algorithm, developed in Section IV-B2, was implemented and tested in a path tracking scenario. For these tests, the controller gains were obtained by using a pole-placement algorithm similar to [21] and initially tuned in a simulation environment on the theoretical dynamic model of the system derived in Section III. Afterwards, the control gains were re-tuned in situ once the robot was in the water. Given the close quarter navigation the UX-1 will have to perform, the requirements of the control tuning was focused on achieving zero error in steady-state with minimal overshoot, with no requirement on rise time or settling time since the operational velocity is quite low.

Fig. 17 shows the overall results of the path tracking underwater test with the feedback linearization control algorithm. As can be seen, the experiment lasted approximately 170s during which the controller was sent a reference path composed of 4 waypoints (x and y in meters, ψ in degrees): $[x, z, \psi] = [(5, -0.2, 0), (5, 2, 0), (2, 2, 0), (2, 0, 0)]$.

The recorded experimental measurements from the localization module are shown for North (Fig. 17(b)), Depth (Fig. 17(c)), Heading (Fig. 17(d)), Roll and Pitch (Fig. 17(e)) and the force commands generated by the control algorithm (Fig. 17(f)). Furthermore, the complete 3D path navigated by the UX-1 robot is shown in Fig. 17(a).

2) PATH TRACKING FINITE HORIZON LQR CONTROL

The Finite Horizon LQR control system is based on the dynamic model in (5) and (6). Given that the pitch angle in these initial tests was to be fixed at 0°, no singularities would be encountered, therefore the system was parametrized with Euler angles as in (29) and (30). Furthermore, the vehicle was considered with a fixed mass and with a fixed position of the center of mass in the standard configuration.

As in the previous section, the controller was initially tuned in a simulation environment with the theoretical and identified model parameters. Using (40), the maximum acceptable steady-state error for each state is used as the requirement

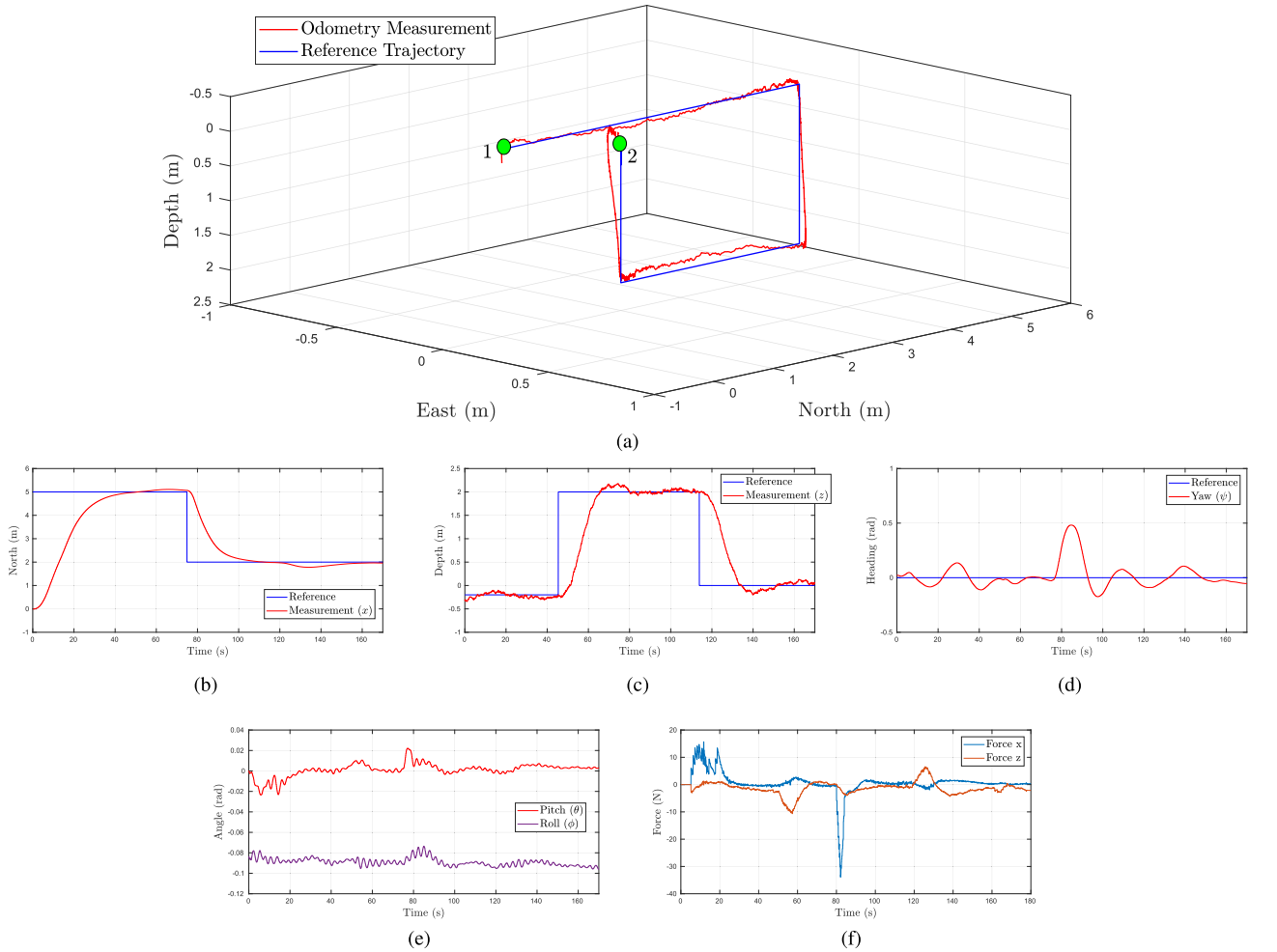

FIGURE 17. Experimental results obtained in underwater tests with the feedback linearization controller: (a) 3D reference path and tracking results (1. start point, 2. end point), (b) north (surge) reference position, (c) depth (heave) references and measurements, (d) heading (yaw) measurements, (e) *Pitch* (θ) and *Roll* (ψ) measurements and (f) commanded forces in *X* and *Z*.

for the state gains; whilst the control weight requirements are constrained to lower control forces. Finally, the robot was manually tuned for the best response once in the test tank.

In order to compare the performance of both control algorithms developed in this work, the path reference commanded to the LQR controller is similar to the one used for the aforementioned feedback linearization controller. The experiment lasted approximately 220s during which the controller was sent a reference path composed of 4 waypoints (x and y in meters, ψ in degrees): $[x, z, \psi] = [(4.5, 0.2, 0), (4.5, 2, 0), (2, 2, 0), (2, 0, 0)]$. In Fig. 18 the results of the underwater control tests are presented for North (Fig. 18(b)), Depth (Fig. 18(c)), Heading (Fig. 18(d)), Roll and Pitch (Fig. 18(e)), Force (Fig. 18(f)), and the 3D path navigated in Fig. 18(a).

VI. RESULTS AND DISCUSSION

In this section, all the experimental results including the identification and control tests, presented in Section V, are analyzed. The first experimental tests were conducted to identify and validate the dynamic model parameters of the UX-1 robot. The thruster coefficient k_m, from (38), was estimated using a load cell to relate the thrust force generated to a commanded RPM velocity. Using the characteristic curve (see Fig. 13), the thruster motor coefficient was estimated as $k_m = 5.9 \times 10^{-8}$.

Analyzing the experimental data from the *BLDC tool*, it is possible to assume that the actuator model, including the velocity loop, follows a first order system. In addition, noticing that the settling time was less than 100ms, it is possible to estimate the time constant of the system to be less than 25ms. For these reasons, the dynamics of the actuators can be safely considered negligible with respect to the ones of the vehicle, and the actuators can be modeled as an instantaneous source of thrust.

As surge will be the predominant motion of the robot during missions, it was important to accurately replicate it within the model. From the identification experiments performed for the surge linear and quadratic damping terms, in Fig. 14, it is apparent that the model in (52) (where both the linear and

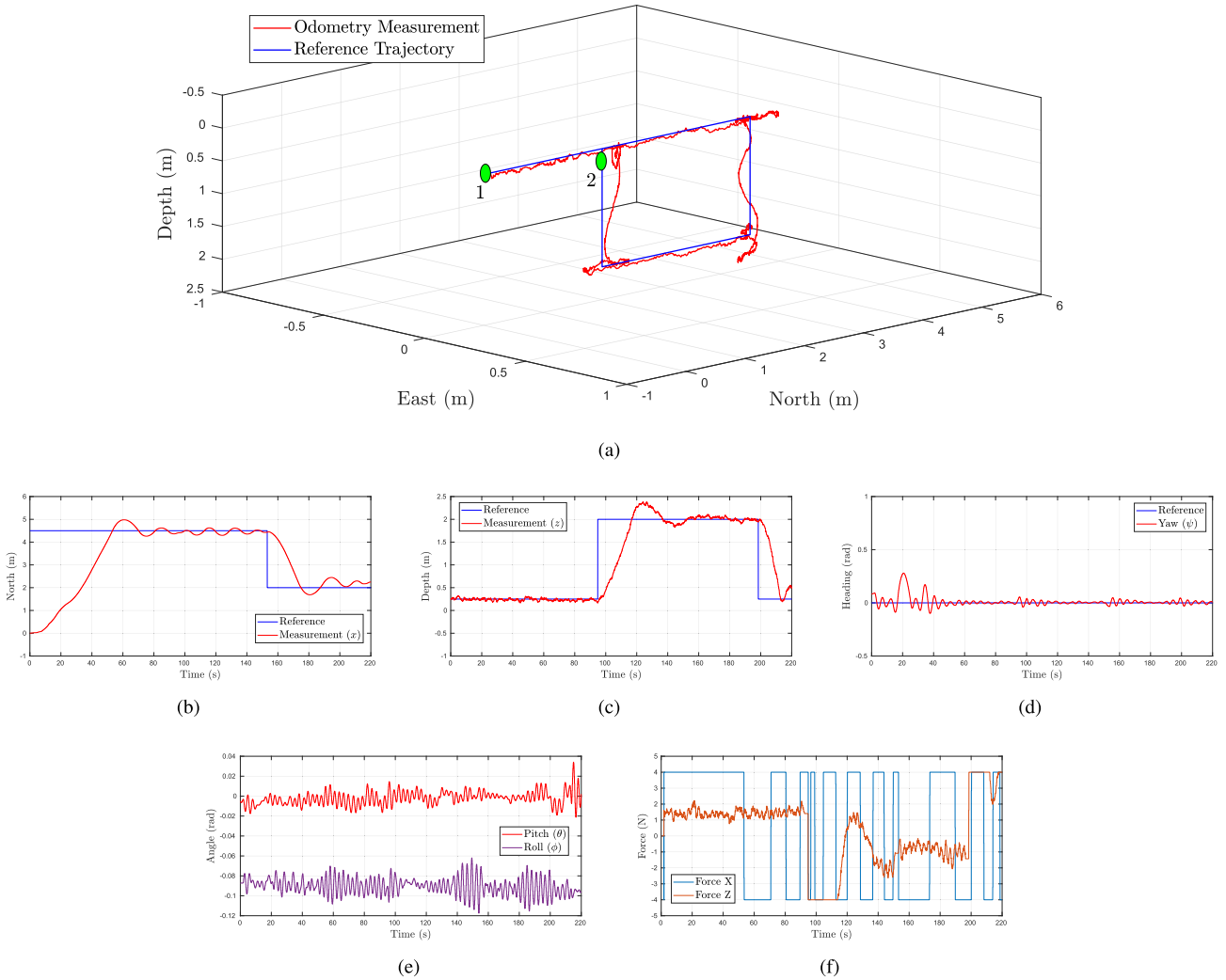

FIGURE 18. Results obtained with the LQR controller: (a) 3D reference path and tracking results (1. start point, 2. end point), (b) north (surge) reference position, (c) depth (heave) measurements, (d) heading (yaw) measurements, (e) *Pitch* (θ) and *Roll* (ψ) measurements and (f) commanded forces in X and Z.

quadratic terms are present) was able to better replicate the vehicle dynamics either in transient and at steady-state.

The fitting percentage of the experimental data to both models was computed by means of the normalized root mean square error (NMRSE). The surge model in (52) obtained a 69.17% fit, 8% higher than the simplified surge model in (51). Using the experimental data, the quadratic drag term results in $X_{|u|u}$ = -73.51 $\pm$ 5.1 kg/m, whereas the linear drag term is estimated as X_u = -65.5 $\pm$ 3.2 kg/m. Furthermore, the theoretical value of the quadratic drag term, calculated using (19), results in $X_{|u|u}$ = -71.13 kg/m showing that the quadratic drag coefficient identified with these experiments is consistent with the theoretical value.

Similarly, the rolling drag parameters were also identified with experimental data. As can be seen in Fig. 16, both models (54) and (55) produce similar results to the experimental data with a fit percentage of approximately 81.09%. In this particular case, the addition of the linear term M_q does not provide any significant improvement, thus the more complex model in (55) is redundant. The identified parameter for the quadratic model has the following value: $M_{|q|q}$ = - 2.76 $\pm$ 0.21 kg·m^2. Table 2 shows the final parameters of the system with both theoretical and identified values.

Following the identification experiments, the controllers developed for the UX-1 robot were tested in real underwater path tracking tests. The path references consisted in several waypoints which simulated a possible mine tunnel navigation scenario. Although the waypoints commanded were not the same, a fair comparison can still be made. As mentioned in previous sections, only the preeminent motions of the UX-1 robot were tested, namely surge, heave and yaw; thus maintaining the pitch, roll and sway constant.

From the plots shown in Fig. 17 and Fig. 18, it can be seen that the overall response of the feedback linearization controller was more effective in tracking the commanded reference path with less deviations. A key factor in the design

TABLE 2. Dynamic model parameters for the UX-1 robot used for control design and simulation.

Parameter	Value	Units
m	112	[kg]
W	1098,72	[N]
B	1176,0	[N]
I_{xx}	4.03	[kg· m^2]
I_{yy}	4.03	[kg· m^2]
I_{zz}	4.03	[kg· m^2]
X_u	-65.5	[kg/m]
Y_v	-65.5	[kg/m]
Z_w	-65.5	[kg/m]
$X_{\|u\|u}$	-73.51	[kg/m]
$Y_{\|v\|v}$	-73.51	[kg/m]
$Z_{\|w\|w}$	-73.51	[kg/m]
$K_{\|p\|p}$	-2.76	[kg· m^2]
$M_{\|q\|q}$	-2.76	[kg· m^2]
$N_{\|r\|r}$	-2.76	[kg· m^2]
$X_{\dot{u}}$	-56.5	[kg]
$Y_{\dot{v}}$	-56.5	[kg]
$Z_{\dot{w}}$	-56.5	[kg]
$K_{\dot{p}}$	-4.52	[kg· m]
$M_{\dot{q}}$	-4.66	[kg· m]
$N_{\dot{r}}$	-4.42	[kg· m]

of the UX-1 was the operating speed of the robot during missions. Even though open-loop maximum speeds have been measured up to 1.0 m/s, for safety, this value was fixed at a maximum of 0.5 m/s, around which the control systems have been developed. Shown in Table 3 are the maximum measured velocities achieved by the UX-1 during testing.

TABLE 3. Velocity results in path tracking experiments with LQR and FL controllers.

Max Velocity	LQR	FL	Units
Forward	0.15	**0.24**	[m/s]
Backward	-0.17	**-0.26**	[m/s]
Downward	**0.145**	0.10	[m/s]
Upward	**-0.15**	-0.09	[m/s]

Since the UX-1 is not a perfect sphere, the performance of the control systems will vary depending on the direction of motion (forward, backward, upward, downward), thus, the velocity in every direction is reviewed. As can be seen, the feedback linearization controller achieves much faster velocities in forward/backward motions as opposed to faster velocities in upward/downward motions from the LQR controller.

During the testing of the LQR controller, it was noticed that the performance of the Depth control was oscillatory and showed a limit cycle around the target reference heave position. The reason behind the oscillations was identified as generated by the low robustness of the control. In details, this test is performed in condition of non perfect neutral bouyancy of the vehicle, in turn keeping the UUV positively buoyant as a safety measure. On the contrary, the heave control is linearized around a condition of perfectly buoyancy, meaning that the model used is not the one representing the system in this specific test scenario and proving that the change on this model parameter is not counteracted by the control system.

Comparing the yaw response from both controllers (Fig. 17(d) and Fig. 18(d)), the faster velocity in the backward motion from the feedback linearization causes an error in the yaw angle which is not seen in the response of the LQR controller, nevertheless, the yaw angle with the feedback linearization control is able to stabilize to the commanded angle of 0° within a reasonable time.

TABLE 4. Force reference commands obtained by the LQR and FL controllers.

	LQR		FL		
Force	North (x)	Depth (z)	North (x)	Depth (z)	Units
Mean	3.91	1.96	**1.92**	**1.92**	[N]
Max	**4.0**	**4.0**	33.93	10.68	[N]

Another important factor in the foreseen missions is lowering as much as possible the power consumption from the batteries in order to achieve longer exploring tasks. Table 4 shows the mean and maximum force commands generated by both controllers during the experiments. The feedback linearization controller managed the lowest mean force value in X and Z, while the LQR controller generated much lower maximum force commands, up to 4N. Nevertheless, in Fig. 17(f) it can be seen that the maximum value for the force commands with the feedback linearization controller is due to peaks in the signal when references are changed, during the rest of the experiment the force values are smooth and within reasonable bounds.

TABLE 5. Time response results in path tracking experiments with LQR and FL controllers.

	LQR		FL		
Metrics	North (x)	Depth (z)	North (x)	Depth (z)	Units
OS%	10.61	22.02	**2.16**	**7.89**	[%]
T_r	36.97	15.99	**18.50**	**12.15**	[s]
T_f	**14.64**	**9.36**	15.90	12.12	[s]
T_s	78.78	54.35	**38.24**	**36.34**	[s]
eSS	0.1045	0.0439	**0.0733**	**0.0351**	[m]

Table 5 presents the results for the transient and steady-state time response analysis of both the feedback linearization and the Finite Horizon LQR controllers. The chosen time response metrics were: Overshoot percentage ($OS\%$), Rise time (T_r), Fall time (T_f), Settling time (T_s) and mean error in Steady-State (eSS).

In a comparison of the time response analysis in Table 5, it is evident that the LQR controller, despite having achieved

a fall time of 9.36s in Depth (2.76s faster than the FL controller), is outperformed in every metric analyzed. The feedback linearization controller managed overshoot percentages of 2.16% in North and 7.89% in Depth, respectively, 8.45% and 14.13% lower than the LQR controller. Additionally, the rise time obtained by the feedback linearization controller is close to twice as fast in North whilst maintaining a significantly lower settling time. Nevertheless, both controllers accomplished very desirable errors in steady-state with a minimum error of 0.0351m in depth for the feedback linearization controller. These errors are acceptable within the bounds of navigating inside the mine tunnel environments, thus, both controllers are suitable for field testing.

VII. CONCLUSION

In this paper the design and realization of the attitude control system for the UX-1 robot, a novel spherical underwater vehicle for flooded mine tunnel exploration characterized by an innovative manifold system for propulsion and maneuvering, has been presented. This process includes the design of the vehicle, the selection of sensors and actuators, the derivation and experimental validation of a 6 DOF dynamic model, and the development and testing of two control solutions for the navigation of the robot. In particular, a linear trajectory tracking controller based on feedback linearization, and a finite horizon LQR based on a linear approximation of the motion equations have been presented and compared.

Underwater tests in a controlled water tank environment have been carried out to experimentally identify model parameters and to validate the proposed controllers in path tracking tests. Experimental results show the effectiveness of both control solutions, emphasizing that the feedback linearization approach outperforms the finite horizon LQR in almost all the considered performance index.

Future work includes the implementation of more advanced control systems, e.g. model predictive control (MPC) or controllers robust to parameter uncertainties, such as $\mathcal{L}_1$ Adaptive Control. Additionally, the controllers proposed in this work will be validated in real mine environments during field tests at the Kaatiala mine in Finland and the Idrija Mercury mine in Slovenia.

REFERENCES

[1] *Securing Essential Imports for the EU—Through Current EU Trade and Related Policies*, Opinion of the European Economic and Social Committee, Official Journal of the European Union, Brussels, belgium, pp. 47–53, 2014.

[2] UNEXMIN.eu. (2016). *Project Overview: Developing Science and Technology*. Accessed: Mar. 1, 2018. [Online]. Available: http://www.unexmin.eu/the-project/project-overview/

[3] J. Yuh, G. Marani, and D. R. Blidberg, "Applications of marine robotic vehicles," *Intell. Service Robot.*, vol. 4, p. 221, Oct. 2011.

[4] S. Nadis, "'Real-time' oceanography adapts to sea changes," *Science*, vol. 275, no. 5308, pp. 1881–1882, 1997.

[5] X. Yu, T. Dickey, J. Bellingham, D. Manov, and K. Streitlien, "The application of autonomous underwater vehicles for interdisciplinary measurements in Massachusetts and Cape Cod Bays," *Continental Shelf Res.*, vol. 22, no. 15, pp. 2225–2245, 2002.

[6] K. B. Ånonsen, O. K. Hagen, and E. Berglund, "Autonomous mapping with AUVs using relative terrain navigation," in *Proc. OCEANS Anchorage*, Anchorage, AK, USA, 2017, pp. 1–7.

[7] C. Roman and H. Singh, "A self-consistent bathymetric mapping algorithm," *J. Field Robot.*, vol. 24, nos. 1–2, pp. 23–50, 2007.

[8] J. Yuh *et al.*, "Design of a semi-autonomous underwater vehicle for intervention missions (SAUVIM)," in *Proc. Int. Symp. Underwater Technol.*, Tokyo, Japan, 1998, pp. 63–68.

[9] D. Youakim, A. Dornbush, M. Likhachev, and P. Ridao, "Motion planning for an underwater mobile manipulator by exploiting loose coupling," in *Proc. IEEE/RSJ Int. Conf. Intell. Robots Syst. (IROS)*, Madrid, Spain, Oct. 2018, pp. 7164–7171.

[10] R. Marthiniussen, K. Vestgard, R. A. Klepaker, and N. Storkersen, "HUGIN-AUV concept and operational experiences to date," in *Proc. Oceans MTS/IEEE Techno-Ocean*, Kobe, Japan, Nov. 2004, pp. 846–850.

[11] S. A. Watson, D. J. P. Crutchley, and P. N. Green, "The design and technical challenges of a micro-autonomous underwater vehicle (μAUV)," in *Proc. IEEE Int. Conf. Mechatronics Automat.*, Beijing, China, Aug. 2011, pp. 567–572.

[12] S. A. Watson and P. N. Green, "Design considerations for micro-autonomous underwater vehicles (μAUVs)," in *Proc. IEEE Conf. Robot., Automat. Mechatronics*, Singapore, Dec. 2010, pp. 429–434.

[13] A. Agrawal, B. Prasad, V. Viswanathan, and S. K. Panda, "Dynamic modeling of variable ballast tank for spherical underwater robot," in *Proc. IEEE Int. Conf. Ind. Technol. (ICIT)*, Cape Town, South Africa, Feb. 2013, pp. 58–63.

[14] C. Yue, S. Guo, M. Li, and Y. Li, "Passive and active attitude stabilization method for the spherical underwater robot (SUR-II)," in *Proc. IEEE Int. Conf. Robot. Biomimetics (ROBIO)*, Shenzhen, China, Dec. 2013, pp. 1019–1023.

[15] Y. Li, S. Guo, and Y. Wang, "Design and characteristics evaluation of a novel spherical underwater robot," *Robot. Auton. Syst.*, vol. 94, pp. 61–74, Aug. 2017.

[16] H. T. Choi, A. Hanai, S. K. Choi, and J. Yuh, "Development of an underwater robot, ODIN-III," in *Proc. IEEE/RSJ Int. Conf. Intell. Robots Syst. (IROS)*, Oct. 2003, pp. 836–841.

[17] R. A. S. Fernandez, E. A. Parrar, Z. Milosevic, S. Domínguez, and C. Rossi, "Design, modeling and control of a spherical autonomous underwater vehicle for mine exploration," presented at the Int. Conf. Intell. Robots Syst. (IROS), Madrid, Spain, Oct. 2018.

[18] J. Vill *et al.*, "Mechanical subsystems integration and structural analysis for the autonomous underwater explorer," in *Proc. IEEE/RSJ Int. Conf. Intell. Robots Syst. (IROS)*, Madrid, Spain, Oct. 2018.

[19] S. Zavari, A. Heininen, J. Aaltonen, and K. T. Koskinen, "Early stage design of a spherical underwater robotic vehicle," in *Proc. IEEE 20th Int. Conf. Syst. Theory, Control Comput. (ICSTCC)*, Oct. 2016, pp. 240–244.

[20] A. Martins *et al.*, "UX 1 system design—A robotic system for underwater mining exploration," in *Proc. IEEE/RSJ Int. Conf. Intell. Robots Syst. (IROS)*, Madrid, Spain, Oct. 2018, pp. 1494–1500.

[21] T. I. Fossen, *Handbook of Marine Craft Hydrodynamics and Motion Control*. Hoboken, NJ, USA: Wiley, 2011.

[22] Society of Naval Architects and Marine Engineers, *Nomenclature for Treating the Motion of a Submerged Body Through a Fluid* (Technical and Research Bulletin). New York, NY, USA: Society of Naval Architects and Marine Engineers, 1950.

[23] T. I. Fossen, "Nonlinear modelling and control of underwater vehicles," Ph.D. dissertation, Dept. Eng. Cybern., Norwegian Univ. Sci. Technol., Trondheim, Norway, 1991.

[24] R. D. Blevins and R. Plunkett, "Formulas for natural frequency and mode shape," *J. Appl. Mech.*, vol. 47, no. 2, pp. 461–462, 1980.

[25] F. H. Imlay, "The complete expressions for added mass of a rigid body moving in an ideal fluid," Armed Services Tech. Inf. Agency, Richmond, VA, USA, Tech. Rep. 1528, 1961.

[26] T. J. Prestero, "Verification of a six-degree of freedom simulation model for the REMUS autonomous underwater vehicle," Ph.D. dissertation, Massachusetts Inst. Technol., Cambridge, MA, USA, 2001.

[27] S. K. Choi and J. Yuh, "Experimental study on a learning control system with bound estimation for underwater robots," in *Underwater Robots*. Boston, MA, USA: Springer, 1996.

[28] M. Ueno, "Hydrodynamic derivatives and motion response of a submersible surface ship in unbounded water," *Ocean Eng.*, vol. 37, no. 10, pp. 879–890, 2010.

[29] G. Antonelli and A. Leonessa, "Underwater robots: Motion and force control of vehicle-manipulator systems," *IEEE Control Syst. Mag.*, vol. 28, no. 5, pp. 138–139, Oct. 2008.
[30] Y. Chen and J. Wang, "A global optimization algorithm for energy-efficient control allocation of over-actuated systems," in *Proc. Amer. Control Conf. (ACC)*, 2011, pp. 5300–5305.
[31] R. M. Murrey. *NASA Propeller Thrust.* Accessed: Feb. 15, 2019. [Online]. Available: https://www.cds.caltech.edu/~murray/courses/cds110/wi06/lqr.pdf

RAMON A. SUAREZ FERNANDEZ received the B.Sc. degree in electrical engineering from the Universidad de Puerto Rico, Mayaguez, Puerto Rico, in 2009, and the M.Sc. degree in electronic engineering from the Universidad de Zaragoza, Zaragoza, Spain, in 2012. He is currently pursuing the Ph.D. degree in automation and robotics with the Universidad Politécnica de Madrid, Madrid, Spain. As a member of the Computer Vision and Aerial Robotics Group, Center for Automation and Robotics, Universidad Politécnica de Madrid, his research interests include the design and development of robotic platforms, and the implementation of advanced control systems in aerial and underwater robotics.

DAVIDE GRANDE received the B.Sc. and M.Sc. degrees in control engineering from the Politecnico di Milano, Italy, in 2015 and 2018, respectively. He has been with INESC-TEC, Porto, Portugal, since 2018. His research interests include aerial and underwater vehicles modeling, and the development of navigation and guidance control laws.

ALFREDO MARTINS is currently a Professor with the School of Engineering (ISEP), Porto Polytechnic Institute (IPP), and a Research Coordinator with the Robotics and Autonomous Systems Group, INESC TEC, Portugal. He currently participates in various international EU FP7 and H2020 (SUNNY, VAMOS, and UNEXMIN) and national deep sea (TURTLE and SIDENAV) marine robotics research projects. He has a vast experience in mobile robotics, having worked with autonomous robots, since 1993. He has participated in multiple robotic research projects with an extensive list of publications in both land, aerial, underwater, and surface autonomous robots. His research interests include the perception, navigation, control, and coordination of mobile robots with particular emphasis on marine robots.

LUCA BASCETTA was born in Milan, Italy, in 1974. He received the Laurea degree *(cum laude)* in computer science engineering and the Ph.D. degree in information technology from the Politecnico di Milano, Italy, in 1999 and 2004, respectively, where he has been an Associate Professor in automatic control with the School of Industrial and Information Engineering, since 2015. He is currently teaching automatic control and control of mobile robots. His research interests include autonomous vehicle planning and control, robotics, visual servoing, and all the problems related to motion control in general. He has been a Senior Member of the IEEE Robotics and Automation Society, since 2017.

SERGIO DOMINGUEZ received the Ph.D. degree in automatic control and robotics from the Universidad Politécnica de Madrid, Spain, in 1995, where he has been an Associate Professor with the Department of Automation, since 1999. His research interests include the control of robots, computer vision systems, and autonomous robots, with special focus on UAV's and AUV's.

CLAUDIO ROSSI received the Ph.D. degree in computer science from the University of Bologna, Italy, in 2001. He has been a Visiting Researcher with the Leiden Institute of Advanced Computer Science (LIACS), The Netherlands, a Postdoctoral Fellow with the Department of Artificial Intelligence, Universidad Politécnica de Madrid (UPM), and a Visiting Professor with the University Carlos III of Madrid. From 2005 to 2009, he was a Ramon y Cajal Research Fellow with UPM. Since 2009, he has been a Professor with UPM. He has participated in several international research projects, and he has published around 80 papers in scientific journals and international conferences, on the topics of artificial intelligence, robotics, and biomimetics. His research interests, initially centered on nature-inspired search techniques for hard optimization problems, have been later directed toward the applications of artificial intelligence to robotics. Since 2009, his research interests have been directed toward bio-inspired systems, shifting form nature-based (software) search techniques to nature-based physical systems.